Graphene-analogue h-BN coupled Bi-rich $Bi_4O_5Br_2$ layered microspheres for enhanced visible-light photocatalytic activity and mechanism insight

Shanshan Ding[a], Danjun Mao[a], Shaogui Yang[a,b,*], Fei Wang[a], Lingjun Meng[a], Mengshu Han[a], Huan He[b], Cheng Sun[a,*], Bin Xu[c]

[a] State Key Laboratory of Pollution Control and Resource Resource Reuse, School of the Environment Nanjing University, Nanjing, 210023, PR China
[b] School of the Environment, Nanjing Normal University, Nanjing, Jiangsu 210046, PR China
[c] State Key Laboratory of Pollution Control and Resource Reuse, College of Environmental Science and Engineering, Tongji University, Shanghai, 200092, PR China

ABSTRACT

The novel boron nitride coupled Bi-rich $Bi_4O_5Br_2$ layered microspheres (h-BN/$Bi_4O_5Br_2$-LMs) were successfully synthesized via a facile ionic liquid-in-water (IL/W) microemulsion-mediated route. The physical, chemical and optical properties of these heterojunction photocatalysts were thoroughly characterized with X-ray diffraction (XRD), X-ray photoelectron spectroscopy (XPS), scanning electron microscopy (SEM) equipped with energy dispersive X-ray spectrometry (EDS), transmission electron microscopy (TEM) and UV–vis diffuse reflection spectroscopy (DRS). Their photocatalytic activities were primarily evaluated by degradation of 4-*tert*-butylphenol (PTBP), which found 1.0 wt% h-BN/$Bi_4O_5Br_2$-LMs to be the best one. The photocurrent experiments showed that the photocurrent density of 1.0 wt% h-BN/$Bi_4O_5Br_2$-LMs was four times higher than that of pure $Bi_4O_5Br_2$-LMs due to enhanced charge transfer ability of the former. It revealed that the addition of h-BN was in favor of suppressing the photoinduced electron-hole pair recombination of $Bi_4O_5Br_2$-LMs, so as to improve the photocatalytic activity of the composite. $^\bullet O_2^-$ and h^+ were proved to be the main reactive species in the photocatalytic process by scavenger experiments and electron paramagnetic resonance (EPR) spectra. In addition, the photocatalytic mechanism of h-BN/$Bi_4O_5Br_2$-LMs was further elaborated in this work. The probable degradation products were identified by GC–MS. The proposed conjugated addition and oxidation reactions were described to be the main pathways by combining the frontier electron density calculation and GC–MS results.

© 2017 Elsevier B.V. All rights reserved.

1. Introduction

Photocatalysis, as a kind of advanced oxidation technology, has a wide range of research and application in the field of environmental pollution control and energy development [1–5]. Nowadays researches of semiconductor catalysts with highly efficient photocatalytic activity become a hot spot.

During the past few years, bismuth oxybromide (BiOBr) has attracted more and more attention and been considered as a new visible-light photocatalyst for its remarkable optical property and promising industrial application [6,7]. The layered structure characterization of $[Bi_2O_2]^{2+}$ slabs interleaved by double slabs of halogen atoms has highly anisotropic electrical, magnetic and optical properties. Moreover, the internal electrostatic field of $[Bi_2O_2]^{2+}$ and Br^- promotes the separation of photoinduced electron-hole pairs, thus improving photocatalytic properties [8–11]. In addition, the suitable band gap of BiOBr is not only conductive to the absorption of sunlight, but also in favor of the photocatalytic oxidation activity under visible-light irradiation [12]. At the same time, considering the low light absorption efficiency, slow photogenerated carrier migration speed and high photogenerated electron-hole recombination rate of primitive BiOBr, efforts have been focused on exploring new modified ways to promote the photocatalytic activity of pure BiOBr, such as bismuth-rich modification or heterojunction photocatalyst construction [13,14]. The principle of bismuth-rich modification method is based on the bottom position of conduction band (CB) which mainly depends on Bi 6p orbit [15]. The successful preparation of $Bi_4O_5Br_2$ [13,16], Bi_3O_4Br [17] and

$Bi_{24}O_{31}Br_{10}$ [15] can further certify that if an appropriate increase in the Bi content of the material, the conduction band can be shifted negatively [13], thereby reducing the band gap and enhancing the visible-light-driven photocatalytic activity. Besides, the construction of the heterojunction structure is also a means used in recent years to improve the catalytic activity of the pure catalyst. And the existing studies have shown that the heterojunction photocatalyst is favorable for the separation of the photogenerated electron-hole pairs, so that the photocatalytic properties are improved. Many heterojunction photocatalysts, such as g-C_3N_4/BiOBr [18], g-C_3N_4/$Bi_4O_5I_2$ [19,20] and BiOBr/nitrogen doped graphene [21], have been synthesized to enhance the photocatalytic activity of pure catalyst by suppressing the recombination of photoinduced electron-hole pairs. Thus, combined with the advantages of these two modification methods, increasing the content of Bi in CB and constructing heterojunction structure, the heterojunction photocatalyst of $Bi_4O_5Br_2$-LMs layered microsphere is considered to be synthesized for improving the photocatalytic activity of pure BiOBr.

It is well documented that composite photocatalysts, synthesized with the semiconductors that have high surface area, layer structure or hydrophobic property, show a good photocatalytic activity in degradation of contaminants for their absorption ability [22]. The structures of graphitic carbon nitride (g-C_3N_4) and hexagonal boron nitride (h-BN) are similar to the graphene and they have the good performance of graphene-like structure [23–26]. H-BN has potential applications in the field of hydrogen storage material and environmental protection due to its chemical stability, strong anti-oxidation ability, good thermal conductivity properties and so on [27–30]. In addition, h-BN has good electronic capture performance. Some photocatalysts, such as BN/BiOBr [31] and BN/BiOI [32], have enhanced their photocatalytic activity due to the addition of BN, indicating BN is helpful to prevent the rapid recombination of photoinduced electron-hole pairs of pure catalyst. However, considering the poor dispersion of h-BN in water, adding ionic liquid which could serve as solvent and reactant can reduce the concern. Therefore, it is available to the formation of the heterojunction photocatalyst h-BN/$Bi_4O_5Br_2$-LMs.

4-*tert*-Butylphenol (PTBP) with strong chemical stability, which belongs to the alkyphenols (APs), is bioaccumulative and harmful. It is so widely utilized, from daily use (such as detergent, soap and so on) and oil-soluble phenolic resin, to the national defense science. PTBP also occupies an important position in fine chemical area, while the various application results in wide distribution in aquatic environment [33–35]. Briefly, PTBP causes endocrine disruption and metabolic change to aquatic organism [36], and even exhibits toxic effect on human [37,38]. Therefore, it is imminent to find an effective method to remove PTBP. However, in addition to biological degradation [39], the degradation of PTBP with a non-titania photocatalyst utilizing visible-light irradiation has rarely been reported [40] and the systematic analysis of degradation pathway of PTBP in terms of photocatalytic mechanism also is hardly reported.

In this study, the novel boron nitride coupled Bi-rich $Bi_4O_5Br_2$ layered microspheres (h-BN/$Bi_4O_5Br_2$-LMs) were firstly prepared by a facile ionic liquid-in-water (IL/W) microemulsion-mediated method. In this IL/W microemulsion-mediated system, while the ionic liquid 1-Octyl-3-methylimidazolium bromide ([Omim]Br) was used as oil-phase which acted as Br source and dispersing agent at the same time, and the surfactant Triton X-100 (TX-100) could be served as the stabilizer of the IL/W microemulsion [41–44]. Subsequently, these photocatalysts were characterized by many experimental techniques and the theoretical calculation based on the semiconductor energy band theory had been done. Furthermore, photocatalytic activities of the as-prepared catalysts were verified by the degradation of PTBP, Acetaminophen (paracetamol, *N*-acetyl-*para*-aminophenol [APAP]) and Norfloxacin (NOR) under visible-light irradiation. Kinetic analysis and product identification of PTBP were also conducted. At last, combining with the theoretical calculation results, the possible photocatalytic mechanism of h-BN/$Bi_4O_5Br_2$-LMs in visible-light irradiation was further discussed.

2. Experimental

2.1. Materials

The ionic liquid [Omim]Br (1-Octyl-3-methylimidazolium bromide, 99%) was obtained from Shanghai Chengjie Chemical Co. Ltd. The PTBP, APAP and NOR were bought from Aladdin Reagent Co. Ltd. The TX-100 (Triton X-100, *p*-Octyl polyethylene glycol phenyl ether) and commercial BN were purchased from Sinopharm Chemical Reagent Co. Ltd. Other chemicals were all analytical grade with no further purification. Deionized water was used in this study.

2.2. Synthesis of photocatalysts
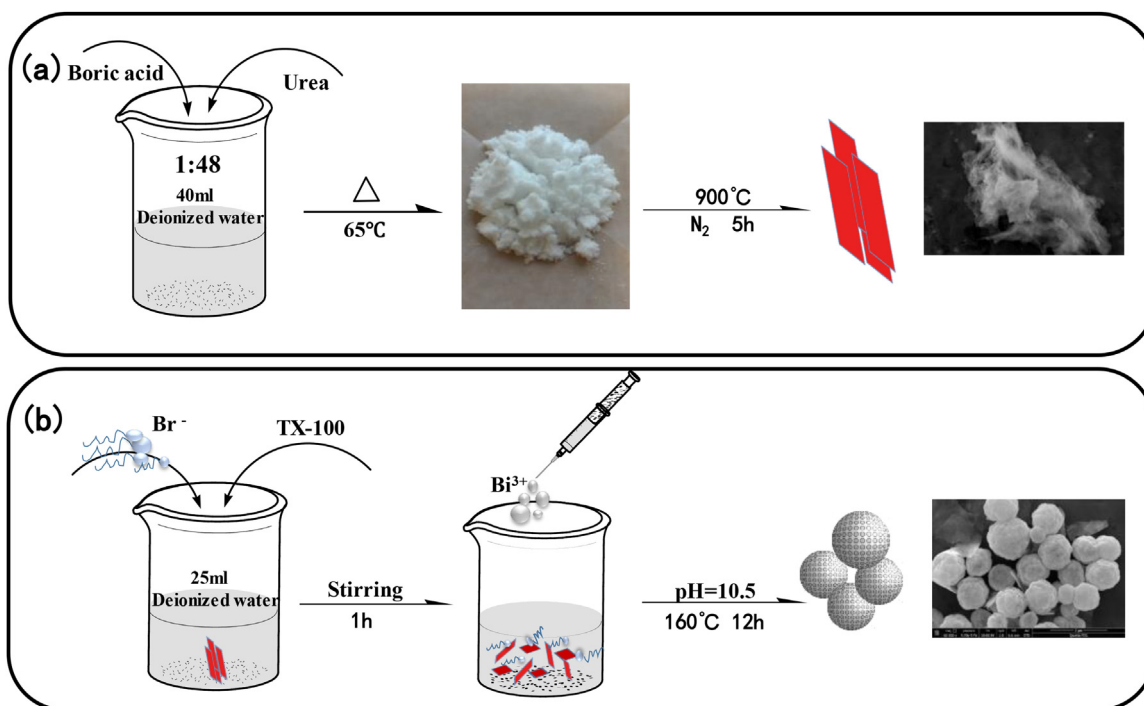
2.2.1. Graphene-analogue h-BN

Graphene-analogue h-BN was synthesized by calcination using boric acid and urea as reactants according to a reported procedure [27]. In a typical synthesis process, the boric acid and urea with the mole ratio of 1:48 were dissolved in 40 ml of deionized water, and the mixed solution was heated at 65 °C. Then the obtained white solid was calcined at 900 °C at a suitable heating rate for 5 h in the nitrogen atmosphere. After cooling to room temperature, the white product was collected and ground into powders.

2.2.2. H-BN/$Bi_4O_5Br_2$-LMs heterostructure photocatalysts

The composites were fabricated via a facile microemulsion-mediated method. In detail, as for the formation of the ionic liquid microemulsion (IL-microemulsion) system, 0.56 g [Omim]Br and 0.2 g TX-100 were dissolved in 25 ml deionized water which contained a certain amount of h-BN (0.2, 0.8, 1.0, 1.5, 2.5 wt%) under vigorous stirring for 3 h. Then the stoichiometric amount of $Bi(NO_3)_3\cdot5H_2O$ was dissolved into 5 ml of dilute nitric acid (1 M). Subsequently, the mixed $Bi(NO_3)_3\cdot5H_2O$ solution was added into the IL-microemulsion system by dropping under continuously stirring, and a yellow homogeneous solution was obtained. After that, the pH was adjusted with NaOH (2 M) to 10.5 and the hybrid solution was maintained stirring for another 1 h at room temperature. Finally, the suspension was transferred into a 50 ml Teflon-lined autoclave and placed at 160 °C in an oven for 12 h. The as-prepared precipitate was washed with deionized water and ethanol for several times, dried at 60 °C for 24 h. The synthetic process of as-prepared samples is vividly displayed in Scheme 1.

2.3. Characterizations

Crystallinity of the as-prepared samples was determined by X-ray diffraction (XRD) on a Bruker D8 Advance (Bruker AXS, Germany) X-ray powder diffractometer with Cu Kα radiation at a setting of 40 kV and 40 mA. X-ray photo-electron spectroscopy (XPS) measurements were conducted on a PHI5000 Versa Probe electron spectrometer (ULVAC-PHI, Japan) equipped with monochromatized Al-Kα radiation. The scanning electron microscopy (SEM) was used to investigate the morphology characteristics of the samples on QUANTA FEG 250 with an energy-disperse X-ray spectroscope (EDS) and transmission electron microscopy (TEM) was operated on JEM-200CX at an acceleration voltage of 200 kV. The specific surface areas were analyzed on Brunauer-Emmett-Teller analysis (BET, ASAP 2020, Micromeritics, USA) with nitrogen adsorption-desorption isotherm at 77 K. The Barrett-Joyner-Halenda (BJH) method was used to calculate

Scheme 1. Schematic illustration of the synthetic process for (a) graphene-analogue h-BN and (b) h-BN/Bi$_4$O$_5$Br$_2$-LMs composites.

pore size. UV–vis diffuse reflectance spectroscopy (DRS) measurements were carried out using a UV-3600 spectrophotometer by taking BaSO$_4$ as a reference. Electron paramagnetic resonance (EPR) spectra were recorded on an EMX-10/12 (Bruker, Germany) with a 500 W Xenon lamp and a 420 nm cut-off filter at room temperature. Moreover, 5, 5-dimeyhyl-1-pyrroline-N-oxide (DMPO) was used as the spin trap in water and methanol, respectively. Electrochemical impedance spectroscopy (EIS) and photocurrent measurement were conducted on an electrochemical system (Shanghai, China) with a standard three-electrode system. The platinum electrode was used as the counter electrode, and saturated Ag/AgCl electrode was as the reference electrode, respectively. 0.02 g as-prepared sample was dissolved in 3 ml ethanol. After ultrasonic treatment, the mixture solution was dip-coated onto ITO glass electrode, and the formed film electrodes were worked as the working electrode. The EIS and photocurrent experiment were both measured with Na$_2$SO$_4$ electrolyte (0.2 M). A 500 W Xenon lamp was used as the light source.

2.4. Photocatalytic studies

The photocatalytic activities of the as-prepared photocatalysts were verified by degrading refractory organic pollutants, including PTBP (10 mg/L), APAP (10 mg/L) and NOR (10 mg/L), under visible-light irradiation. The simulated visible-light experiments were conducted on a photochemical reaction instrument (XPA-7, Nanjing, China) equipped with 1000 W Xenon lamp. The photocatalytic experiments were described as follows: 50 mg catalyst was dispersed into 50 ml solution containing the targeted pollutant. To eliminate the effect of the adsorption, the suspension was continuously stirred for an hour under dark. When the adsorption-desorption equilibrium attained in dark, light illumination started. Adding a 420 nm cut-off filter was to remove light of λ < 420 nm. During the irradiation process, 4 ml of the suspension was taken from the reaction colorimetric tube, centrifuged and filtered using a 0.22 μm Millipore filter to remove the particle. Subsequently, the concentration of solution was examined by a UV–vis spec-

troscopy (Lambda-750, PerkinElmer). To verify the stability and reproducibility of as-synthesized catalysts, duplicate runs were performed under the same condition.

2.5. Analytical methods

The concentration of PTBP was measured by a UV–vis spectrophotometer, and accurately validated by using an Agilent 1200 high performance liquid chromatography (HPLC) with a UV detector and a C18 reversed phase column (5 μm, 4.6 × 150 mm). Through calculation, the activity of catalyst could be intuitively performed by degradation efficiency of PTBP. In the HPLC analysis, methanol-water (7:3, v/v) was used as the mobile phase at 1 ml/min and detection of PTBP was at wavelength of 274 nm. The injection volume for each sample was 20 μl.

The degradation products of PTBP were analyzed by gas chromatography-mass spectrometer (GC–MS) equipped with a TG-5SILMS column (30 m × 0.25 mm × 0.25 μm). Before GC–MS analysis, centrifugation of the reaction solution was to remove the particle. The obtained solution was acidified with HCl (1 M) to pH 2–3 and extracted with an equal volume of ethyl acetate-n-hexane (2:1, v/v) for three times. The collected organic layer was dried under flowing nitrogen and then was dissolved in 1 ml acetonitrile. In addition, the sample with TMS derivatization was carried out at 60 °C for 2 h with adding 100 μl of bis (trimethylsily) trifluoroacetamide (BSTFA).

For the GC–MS analysis, two temperature programs were set. One was for no derivatization samples, and the other was for TMS derivatization samples. The former approach was as follows: the initial temperature of GC was 60 °C and held for 2 min, and then it increased to 300 °C at 5 °C/min and held at 300 °C for 5 min. For the latter, the initial temperature of GC was 90 °C and held for 1 min; subsequently it raised up to 150 °C at a rate of 15 °C/min, then ramped at 300 °C with a rate of 5 °C/min and held for 6 min. The injection, transmission line and ion source temperatures were 280 °C, 280 °C and 250 °C, respectively. Helium was used as the car-
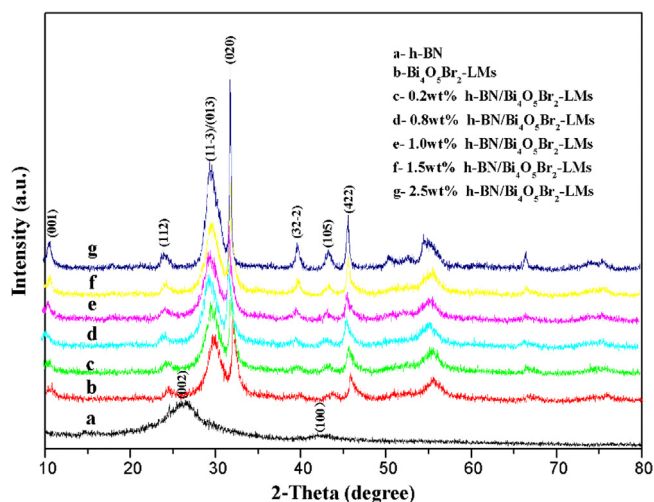
Fig. 1. XRD patterns of $Bi_4O_5Br_2$-LMs and h-BN/$Bi_4O_5Br_2$-LMs composites in different addition amounts of h-BN.

rier gas at 1.0 ml/min. Election impact (EI) mode was utilized and the election energy was set to 70 eV.

2.6. Theoretical calculation of PTBP

The molecular orbital calculation of PTBP was conducted in Gaussian 09 program at B3LYP/6–311 + G* level with a minimum energy. The frontier electron densities (FEDs) of highest occupied molecular orbital (HOMO) and the lowest unoccupied molecular orbital (LUMO) of each atom were calculated. In addition, values of $FED^2_{HOMO} + FED^2_{LUMO}$ were used to predict whether the reaction site is easy attraction of free radicals.

3. Results and discussion

3.1. Characterization of h-BN/$Bi_4O_5Br_2$-LMs

3.1.1. XRD analysis

To analyze the purity and crystalline phase structure of the as-prepared samples with different contents of h-BN, XRD was utilized. In Fig. 1, lines of diverse colors represent various photocatalysts with different addition amounts of h-BN. The diffraction peaks of the sample without the addition of h-BN were indexed to the monoclinic $Bi_4O_5Br_2$-LMs (JCPD card no.37-0699) [13] which at $2\theta = 10.5°, 24.5°, 29.6°, 32.0°, 39.8°, 43.4°, 45.8°$ corresponded to (001), (112), (113-3)/(013), (020), (32-2), (105), (422), respectively. It suggests that a pure crystal phase was formed. Additionally, for the h-BN, two broad diffraction peaks locate at around 26.1° and 42.4° are ascribed to the (002) and (100) crystal planes of h-BN (JCPD card no.34-0421) [45,46]. Although the diffraction peaks lightly shift to the left and the peak strengths increase with the increment of loaded h-BN, the overall patterns of the h-BN/$Bi_4O_5Br_2$-LMs composites with various contents of h-BN are similar to that of pure $Bi_4O_5Br_2$-LMs. No obvious diffraction peaks of h-BN can be found which may be due to low levels of h-BN, the low diffraction intensity and the good dispersion of h-BN in the hybrid materials. The same phenomenon was reported in some literatures [31,32]. Additionally, it can be seen that as the amount of h-BN was added, each diffraction peak intensity of the as-prepared materials also increased and became more and more acute, which indicates that the crystalline of composite photocatalyst becomes better. Furthermore, the diffraction peaks of other impurities are not found in both complex and pure materials, which show that no new crystalline phase generated in the process of preparation. The

above results indicate that the addition of h-BN does not affect the crystalline phase structure of $Bi_4O_5Br_2$-LMs.

3.1.2. XPS analysis

XPS analysis was used to demonstrate the existence of h-BN and the valence states of elements on the surface of h-BN/$Bi_4O_5Br_2$-LMs composite. Fig. 2a depicts the survey scan spectra of pure $Bi_4O_5Br_2$-LMs, 1.0 wt% h-BN/$Bi_4O_5Br_2$-LMs and h-BN. The chemical compositions of the as-synthesized samples including Bi, O, Br, B and N are all observed on the surface of h-BN/$Bi_4O_5Br_2$-LMs. The obvious peak of three samples at approximately 284.6 eV can be seen from the spectra, which may be attributed to the signal from carbon contained in the apparatus and the signal can be used as the correction for specimen [13,47]. High-resolution XPS spectra further suggested the chemical states. Fig. 2b–d shows the high-resolution XPS spectra of Bi 4f, O 1 s and Br 3d, respectively. For h-BN/$Bi_4O_5Br_2$-LMs, the characteristic peaks of the Bi $4f_{7/2}$ and Bi $4f_{5/2}$ are located at 158.5 eV and 163.8 eV, indicating that Bi ions present a valence of +3 in the sample. It is obvious that it happens a 0.4 eV shift to higher binding energy compared with the pure $Bi_4O_5Br_2$-LMs, which suggests the different chemical environment of Bi^{+3} [17]. The O 1 s peaks in Fig. 2c can be fitted with two peaks at around 528.8 eV and 531.6 eV for the pure $Bi_4O_5Br_2$-LMs which attribute to lattice oxygen and surface O—H bonds [16]. Likewise, the characteristic peaks of O 1 s also slightly shift to the left which is in line with the decreased strength, which may be due to the influence of formed heterojunctions between two catalysts or the change of the chemical environment. As shown in Fig. 2d, while the peaks of 67.5 eV and 68.5 eV closely conform to the Br $3d_{5/2}$ and Br $3d_{3/2}$ for $Bi_4O_5Br_2$-LMs, the correspondent characteristic peaks for h-BN/$Bi_4O_5Br_2$-LMs is observed at about 67.9 eV and 69.1 eV. The spectra of B 1 s (Fig. S1a) and N 1 s (Fig. S1b) further demonstrate that h-BN has been successfully attached on $Bi_4O_5Br_2$-LMs via a facile microemulsion-mediated method. In addition, the shifts of the peaks of B1 s and N1 s manifest that the binding interaction between h-BN and $Bi_4O_5Br_2$-LMs has been generated during the microemulsion-mediated process.

3.1.3. SEM and EDS analysis

To further identify the successful synthesis of composite h-BN/$Bi_4O_5Br_2$-LMs, SEM and EDS were characterized. As seen in Fig. 3a, the local morphology of as-prepared h-BN by calcination looks very thin and transparent and is similar to cottony cloud. Fig. 3b–g shows the microscopic outlook of h-BN/$Bi_4O_5Br_2$-LMs with different contents of h-BN. It should be pointed out that the addition of h-BN does not change the morphology and microstructure of the $Bi_4O_5Br_2$-LMs. However, when the loaded amount of h-BN exceeds 1 wt%, miscellaneous pieces of the as-synthesized samples also increase. These results indicate that excess h-BN might affect or even destroy the $Bi_4O_5Br_2$-LMs structure. Unfortunately, as the h-BN flakes conformally cover the nanoparticles, it is relatively hard to claim conformed surface coverage of them from the SEM images due to their ultra-thinness in nature. The results accompanied with XRD analysis indicate that the addition of h-BN was scanty. The same phenomenon has also been reported in other studies [48].

The EDS line scan spectra and elemental mappings can characterize the surface element composition and the distribution of element of the sample. In Fig. 3h, the spectrum of EDS depicts that the as-prepared photocatalyst contains Bi, O, Br, B, and N. Similar phenomena can also be observed in the EDS elemental mapping. From Fig. 4a–g, it can be seen that all elements are distributed uniformly throughout the whole material, but the content varies greatly. It is observed that the highlights of B and N are less for their scarce addition. The above characterization can sufficiently explain
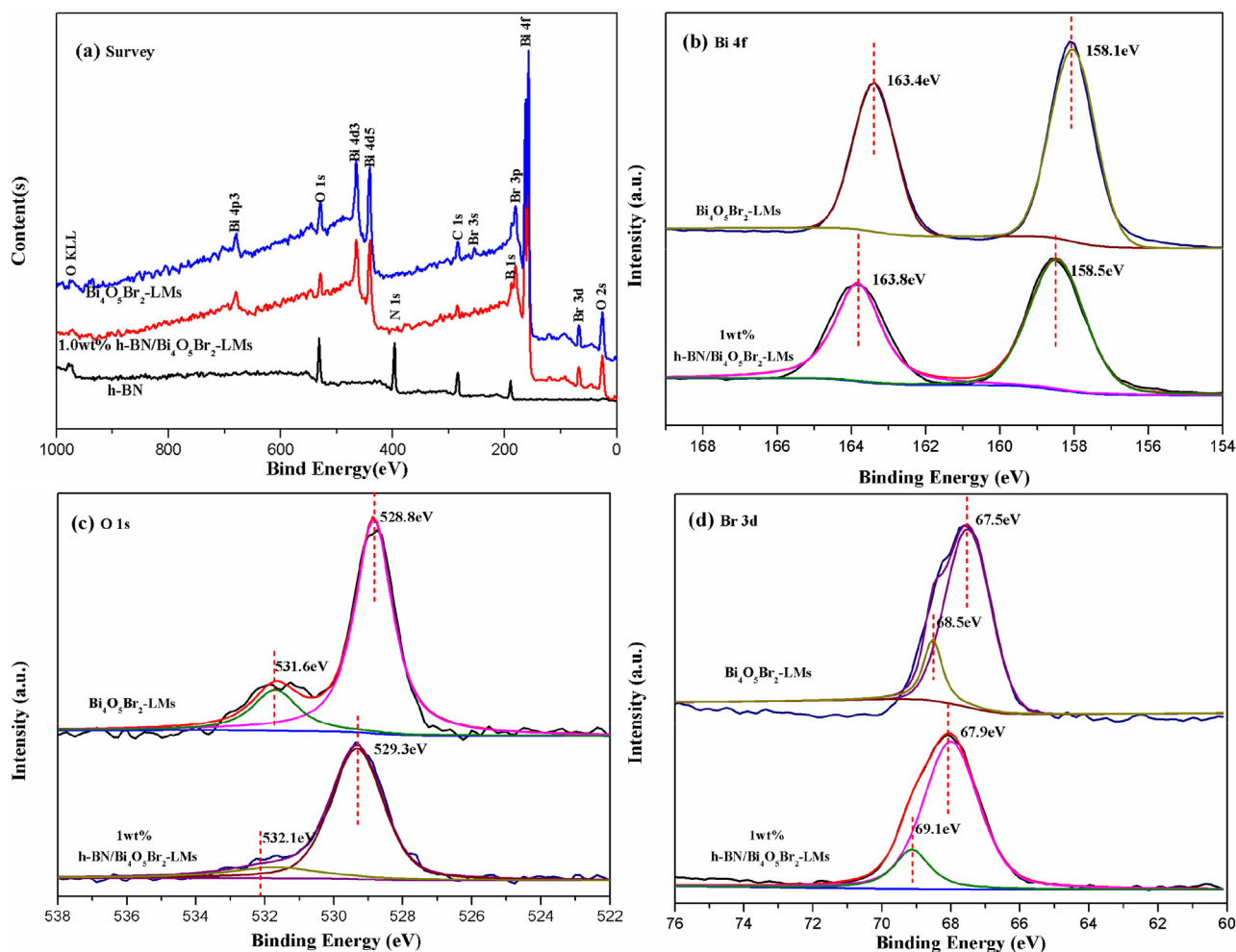
Fig. 2. XPS spectra of as-prepared $Bi_4O_5Br_2$-LMs, h-BN and 1.0 wt% h-BN/$Bi_4O_5Br_2$-LMs. (a) Survey; (b) Bi 4f; (c) O 1 s and (d) Br 3d.

the successful synthesis of the h-BN/$Bi_4O_5Br_2$-LMs and confirm the coexistence of h-BN and $Bi_4O_5Br_2$-LMs in this composite.

3.1.4. TEM and HRTEM analysis

Although surface morphology can be observed by SEM, the microstructural details of the sample need to be investigated by TEM and HRTEM observation. Fig. 5a and b describes the overview of h-BN and h-BN/$Bi_4O_5Br_2$-LMs, respectively. Fig. 5a depicts h-BN very thin and almost transparent. The prepared material having a certain degree of vacuum and layered microsphere structure can also be observed apparently observed in Fig. 5b and 5c. There is certain degree of hollow in the layered microsphere structure which allows light beams to access to its interior diffracted and reflected, thereby improving photon capture rate. HRTEM (Fig. 5d) was emplyed to prove the formation of heterojunction between h-BN and $Bi_4O_5Br_2$-LMs. The image clearly exhibits the h-BN (002) facet with a spacing of 0.33 nm [49] and the spacing of 0.276 nm corresponding well to the (120) facet [13]. The results demonstrate that the heterojunction in h-BN/$Bi_4O_5Br_2$-LMs has been facilely formed.

### 3.1.5. Nitrogen adsorption analysis

The greater the surface area of catalyst, the more active sites of the surface have, which are more conductive to contact organic pollutant on its surface. Thus, the catalytic activity can be improved [50]. Nitrogen adsorption-desorption measurement was utilized to analyze and calculate the specific surface area and pore size of as-

formed photocatalysts. In Fig. S2, the BET specific surface area of pristine $Bi_4O_5Br_2$-LMs is calculated to be 31.36 m^2g^{-1}, while that of h-BN/$Bi_4O_5Br_2$-LMs slightly increases to 32.45 m^2g^{-1}. The tiny gap between the two surface areas demonstrates that the specific surface area may be not the main factor to affect the photocatalytic activity.

3.2. Optical properties of h-BN/$Bi_4O_5Br_2$-LMs

3.2.1. DRS analysis

Another major factor affecting the catalytic activity is light-absorbing property of the sample, which can be characterized by UV–vis diffuse reflectance spectroscopy (DRS) at room temperature. In Fig. 6a, while it can be clearly seen that pure h-BN presents strong absorption at 310 nm, bare $Bi_4O_5Br_2$-LMs is at 480 nm. After the heterojunction is formed between h-BN and $Bi_4O_5Br_2$-LMs, the optical absorption of the composite lightly increases, which may be due to high transmission of h-BN within visible-light region [51]. Furthermore, the theoretical band gap energy (E_g) of the as-prepared sample can be calculated using the equation: $(\alpha h\nu)^n = A(h\nu - E_g)$, where α is the absorption coefficient, h is Planck's constant, ν is light frequency, A is a constant and n is an index which depends on the electronic transition of the semiconductor. n = 2 is for direct-gap semiconductor, n = 1/2 is for indirect-gap one. For h-BN and $Bi_4O_5Br_2$-LMs, n is 1/2 [15,52]. As shown in Figs. 6b and S3a–d, E_g values of $Bi_4O_5Br_2$-LMs loaded with different amounts of h-BN (0 wt%–2.5 wt%) are 2.36 eV, 2.33 eV,
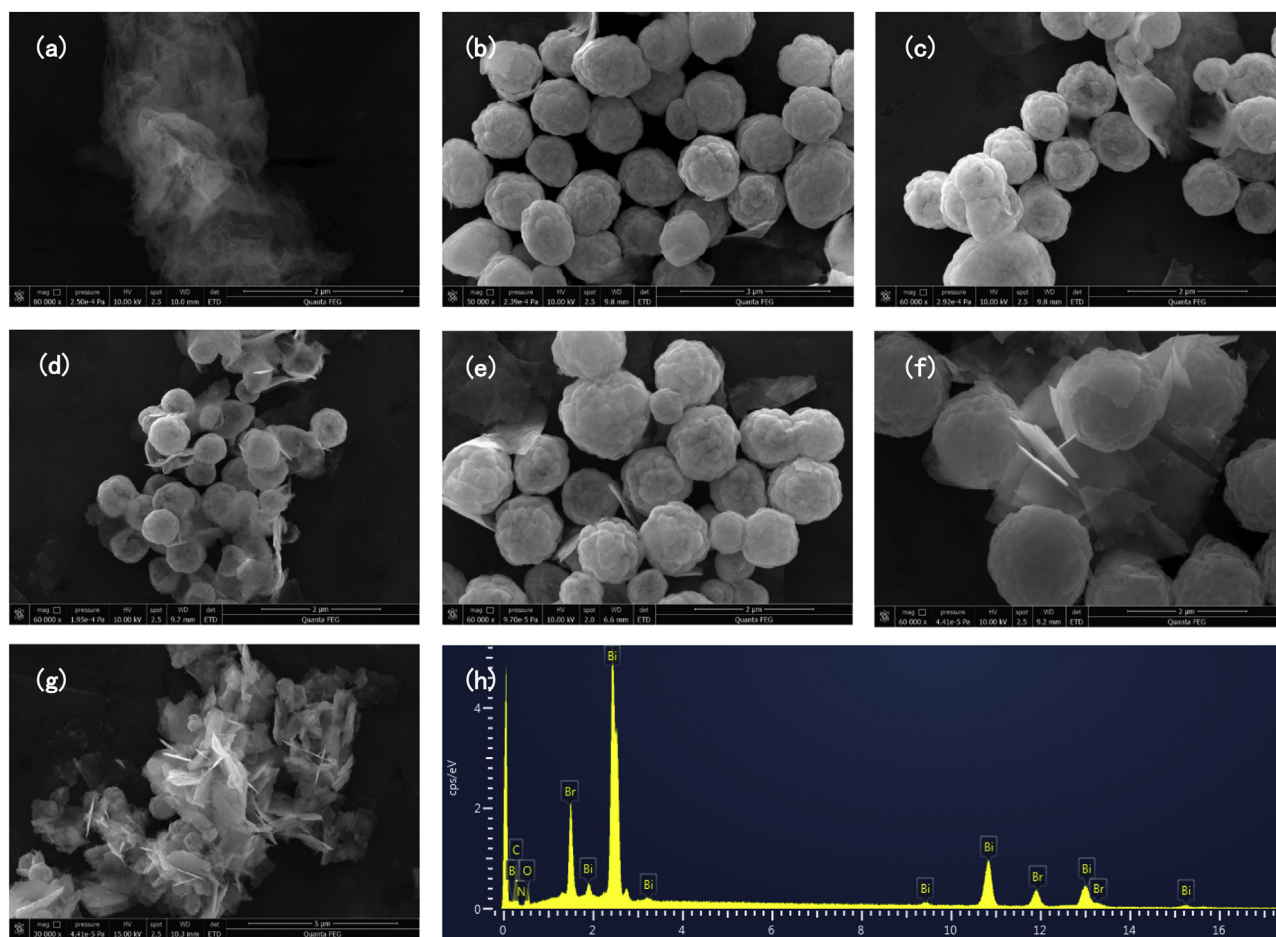
Fig. 3. (a)–(g) the SEM images of h–BN, $Bi_4O_5Br_2$-LMs, 0.2 wt% h–BN/$Bi_4O_5Br_2$-LMs, 0.8 wt% h–BN/$Bi_4O_5Br_2$-LMs, 1.0 wt% h–BN/$Bi_4O_5Br_2$-LMs, 1.5 wt% h–BN/$Bi_4O_5Br_2$-LMs and 2.5 wt% h–BN/$Bi_4O_5Br_2$-LMs; (h) EDS pattern of 1.0 wt% h–BN/$Bi_4O_5Br_2$-LMs.
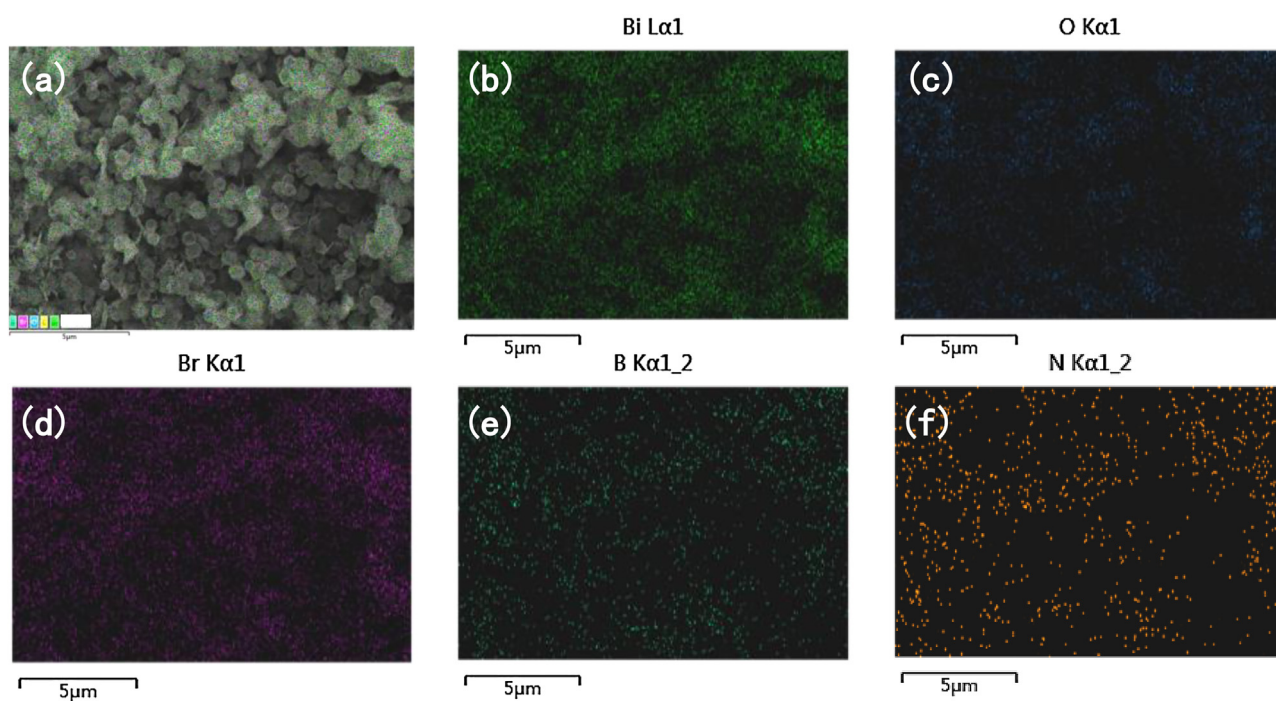
Fig. 4. (a) SEM-EDS elemental mapping of 1.0 wt% h–BN/$Bi_4O_5Br_2$-LMs, (b)-(f) the EDS elemental mapping of Bi, O, Br, B and N.
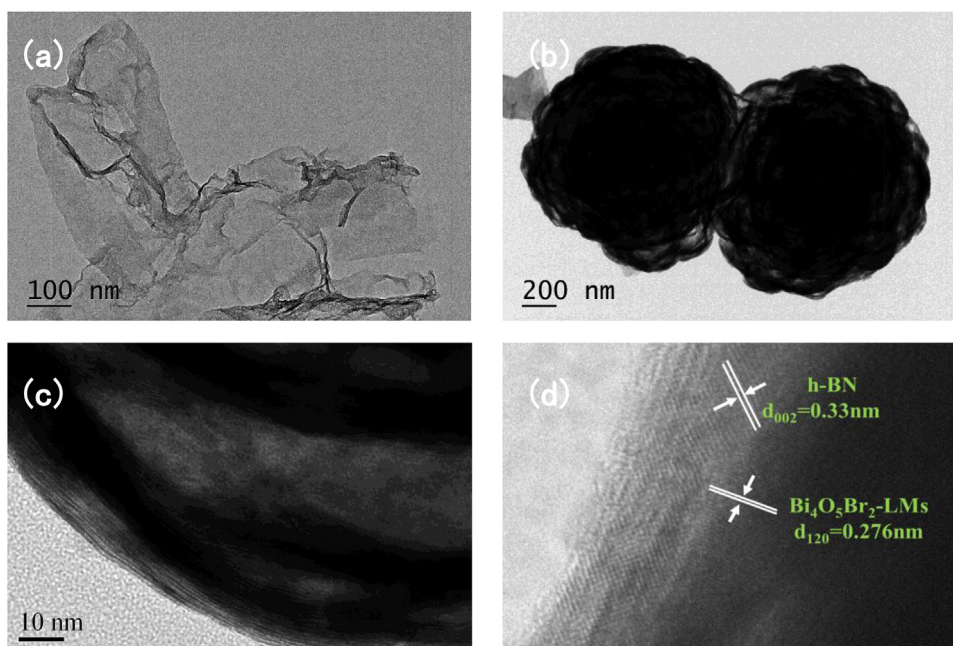
Fig. 5. (a) The TEM image of h-BN; (b) and (c) the TEM image of 1.0 wt% h-BN/Bi$_4$O$_5$Br$_2$-LMs; (d) the HRTEM image of 1.0 wt% h-BN/Bi$_4$O$_5$Br$_2$-LMs.

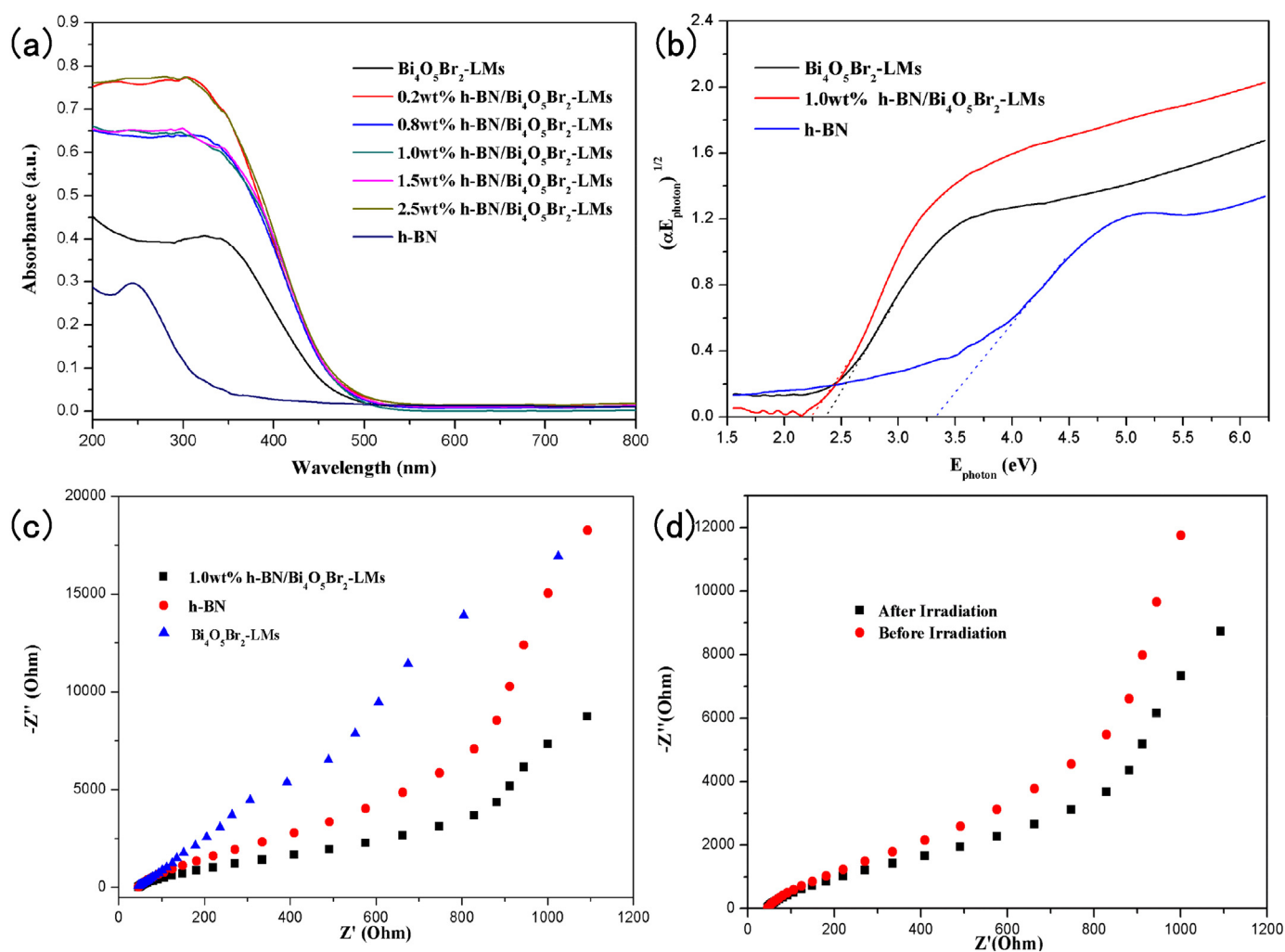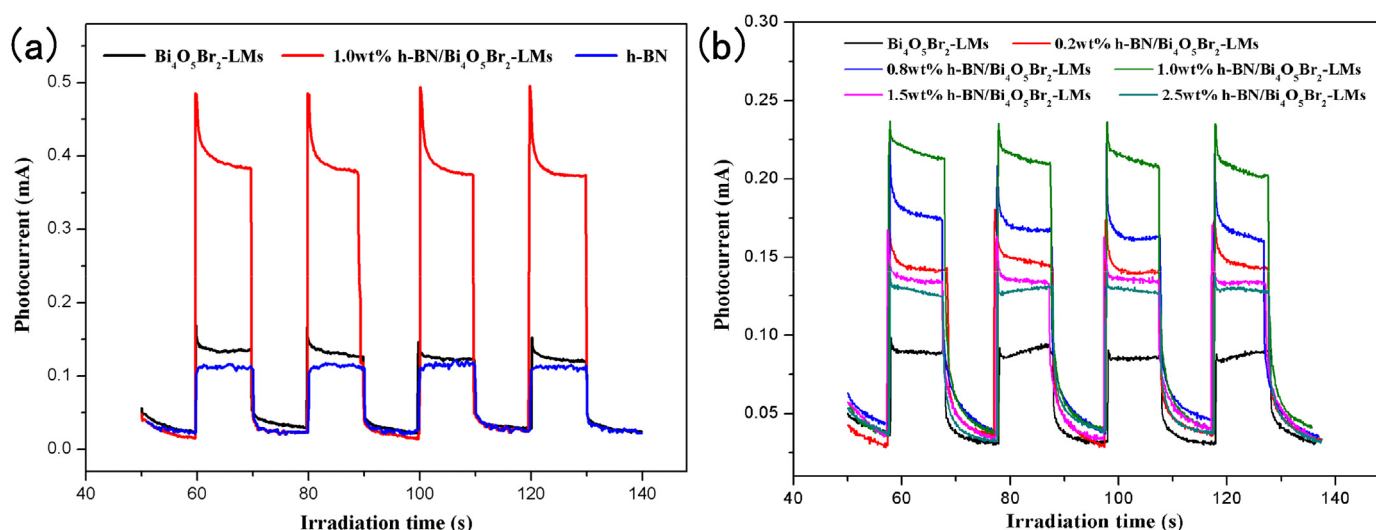**Fig. 6.** (a) The UV–vis diffuse reflectance spectra of the as-prepared samples and (b) (αE$_{photon}$)$^{1/2}$ vs. E$_{photon}$ curves of h-BN, Bi$_4$O$_5$Br$_2$-LMs and 1.0 wt% h-BN/Bi$_4$O$_5$Br$_2$-LMs. Electrochemical impedance spectroscopy (EIS) Nyquist plots of the sample electrodes of (c) 1.0 wt% h-BN/Bi$_4$O$_5$Br$_2$-LMs, pure h-BN and Bi$_4$O$_5$Br$_2$-LMs; (d) 1.0 wt% h-BN/Bi$_4$O$_5$Br$_2$-LMs before and after photocatalytic reaction.

Fig. 7. (a) Photocurrent response for the pure h-BN, $Bi_4O_5Br_2$-LMs and 1.0 wt% h-BN/$Bi_4O_5Br_2$-LMs electrodes under visible-light irradiation; (b) Photocurrent response of the as-prepared composite photocatalysts with different loaded amounts of h-BN in 0.2 M Na_2SO_4 aqueous solution.

2.29 eV, 2.24 eV, 2.34 eV and 2.35 eV, respectively. The E_g value of 1.0 wt% h-BN/$Bi_4O_5Br_2$-LMs is the least one. Furthermore, the calculated band gap energies of composite materials are all lower than that of pure $Bi_4O_5Br_2$-LMs, which indicates that h-BN/$Bi_4O_5Br_2$-LMs can generate more electron-hole pairs under visible-light excitation. But it is worth noting that the E_g values of samples will increase when the loaded amount is excess, which is similar to aforementioned phenomenon that miscellaneous pieces of the as-synthesized sample also increase with loading of h-BN over 1 wt%. Based on the DRS spectra, the subtle differences of E_g indicate that the photon absorption efficiency is not the main factor affecting photocatalytic activity enhancement of h-BN/$Bi_4O_5Br_2$-LMs.

3.2.2. EIS analysis

Electrochemical impedance spectroscopy (EIS) was applied to investigate generated charge transfer impedance. The spectrum consists of a semicircle in the high frequency and an incline straight line in the low frequency region. The semicircle is due to charge transfer impedance, elucidating that the charge transfers through the electrode- electrolyte interface. The smaller diameter of Nyquist circle, the lower resistance generated, which can speed up the transfer process of surface charge [18]. In Fig. 6c, the diameter of the Nyquist circle of 1.0 wt% h-BN/$Bi_4O_5Br_2$-LMs is smaller than those of bare h-BN and $Bi_4O_5Br_2$-LMs, which reveals that h-BN/$Bi_4O_5Br_2$-LMs has a lower interfacial charge-transfer resistance and more effective photoinduced electron-hole pairs separation. Therefore, compared with pure $Bi_4O_5Br_2$-LMs, h-BN/$Bi_4O_5Br_2$-LMs has a better photocatalytic activity which is mainly attributed to the lower electron-hole recombination rate. Furthermore, the spectrum (Fig. 6d) verifies the photocatalytic degradation process of PTBP by 1.0 wt% h-BN/$Bi_4O_5Br_2$-LMs. The measured diameter value of the composite film which is made by the sample before irradiation is larger than that of film illuminated by light. The photocatalytic degradation process is the main reason of impedance decrease under light irradiation. When the contaminants are adsorbed on the catalyst surface after the attained adsorption-desorption equilibrium, the electrons cannot transmit from the contaminant molecules to the electrode, leading a greater resistance [53]. In the photodegradation process, the surface contaminants are degraded. More electrons are injected into the electrode so that impedance decreases.

### 3.2.3. Photocurrent analysis

It is well known that the generation of photocurrent results from the transfer of electron from the conduction band of catalyst to the electrode [18]. Thus the photocurrent intensity indirectly reflects the ability of charge transfer. When the light is on, the photocurrent intensity increases to a stable value immediately, and rapidly returns to dark current state when there is no light illumination. As depicted in Fig. 7a, the maximum photocurrent density of 1.0 wt% h-BN/$Bi_4O_5Br_2$-LMs is approximately four times higher than those of pristine h-BN and $Bi_4O_5Br_2$-LMs under light illumination. Generally speaking, the higher photocurrent intensity represents the higher separation rate of photogenerated electron-hole pairs, demonstrating the photocatalytic activity has been improved [54]. Fig. 7b shows the photocurrent response of the as-prepared composite photocatalysts with different loaded amounts of h-BN. It is clearly seen that all the as-prepared composite photocatalysts show prompt and reproducible photocurrent response. After the introduction of h-BN, the composite catalysts are more favorable than pure $Bi_4O_5Br_2$-LMs in charge separation which resulted in much higher photocatalytic activity. Based on the EIS analysis and photocurrent measurement, the introduction of h-BN greatly suppresses the recombination of electron-hole pairs and enhances the photocatalytic efficiency of the composite catalyst.

3.3. Evaluation of photocatalytic activity

3.3.1. Photocatalytic degradation of pollutants

The photocatalytic activity of as-prepared sample was mainly examined by degrading PTBP under visible-light irradiation. As shown in Fig.S5b, PTBP is eluted after a 4.74 min retention time (RT) and almost disappeared at 150 min, which is in accordance with the UV–vis spectroscopy results. In addition, direct photo-degradation of PTBP without photocatalyst and with the presence of h-BN as a reference object were also investigated (Fig. 8a). To be more specific, the former demonstrated that the self-degradation of PTBP under visible-light almost be neglected and the latter aimed to prove that h-BN had no catalytic degradation effect of PTBP. Compared with pure BiOBr, $Bi_4O_5Br_2$-LMs exhibits better catalytic activity, for example, about 55% of pollutant is photodegraded in 150 min irradiation. When $Bi_4O_5Br_2$-LMs is loaded with a certain amount of h-BN, the photocatalytic degradation activities of the composites are superior to those of bare BiOBr and $Bi_4O_5Br_2$-LMs, indicating that the presence of h-BN has a significant influence on
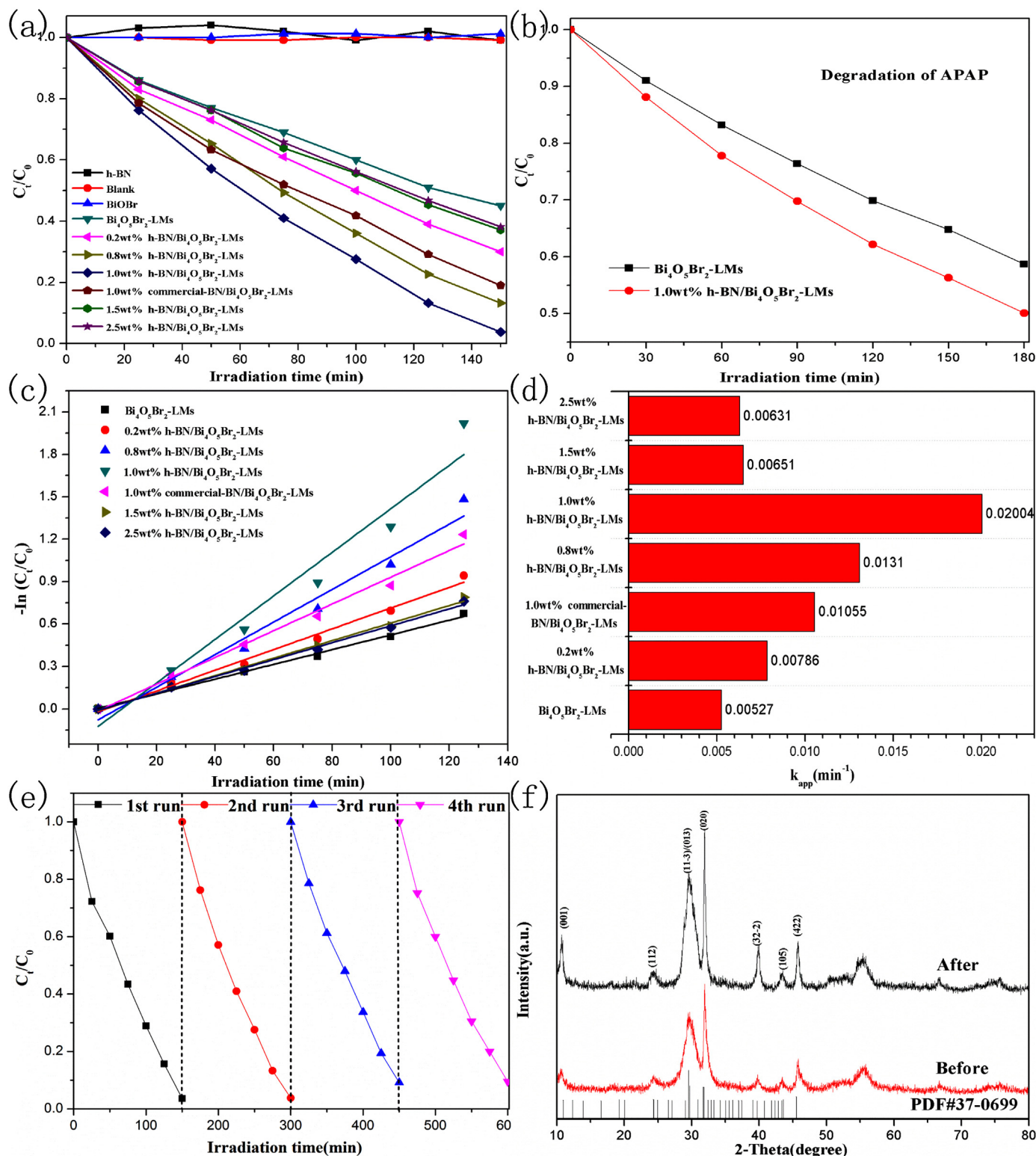
Fig. 8. (a, c, d) Photocatalytic degradation, pseudo-first-order kinetics curves and k_{app} of PTBP (10 mg/L) with adding different catalysts under visible-light irradiation; (b) Degradation of APAP (10 mg/L) in presence of $Bi_4O_5Br_2$-LMs and 1.0 wt% h-BN/$Bi_4O_5Br_2$-LMs catalysts. (e) Recycling properties of the photocatalytic degradation of PTBP with 1.0 wt% h-BN/$Bi_4O_5Br_2$-LMs; (f) XRD patterns of 1.0 wt% h-BN/$Bi_4O_5Br_2$-LMs before and after photocatalytic degradation reaction.

photocatalytic activity. Obviously, the photocatalytic activity of h-BN/$Bi_4O_5Br_2$-LMs increases with the amount of h-BN up to 1.0 wt%, in which 1.0 wt% h-BN/$Bi_4O_5Br_2$-LMs exhibits the best photocatalytic activity with the degradation efficiency of about 97%. The degradation activity of the composite catalyst increases with doped amounts of h-BN but decreases as the content exceeds 1 wt%. Thus the optimum amount of loaded h-BN is 1 wt%. Compared with pristine $Bi_4O_5Br_2$-LMs, too much or too little of the loaded content of h-BN does not significantly enhance the catalytic activity. Therefore, if the amount of h-BN is less than optimum loading, as the
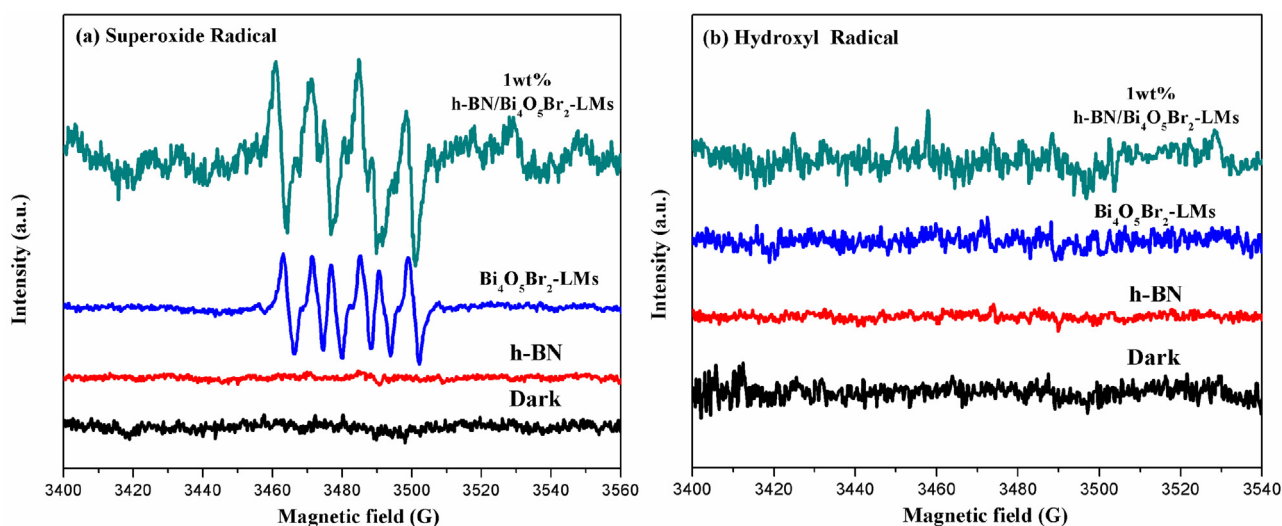
Fig. 9. DMPO spin-trapping EPR spectra recorded with 1.0 wt% h-BN/$Bi_4O_5Br_2$-LMs, pure $Bi_4O_5Br_2$-LMs and h-BN in (a) methanol dispersion and (b) aqueous dispersion under visible-light irradiation.

amount of h-BN increases, the formed heterojunctions between h-BN and $Bi_4O_5Br_2$-LMs intensify, which is more conducive to electron-hole pair separation. Unfortunately, excessive loading of h-BN may cause a decline in terms of degradation activity, because too much h-BN covers the surface active sites of $Bi_4O_5Br_2$-LMs. Besides, the degradation activity of 1.0 wt% h-BN/$Bi_4O_5Br_2$-LMs is obviously higher than that of 1 wt% commercial-BN/$Bi_4O_5Br_2$-LMs due to the few as-prepared h-BN layers (Fig.S4) [27].

The photocatalytic degradation of PTBP follows a pseudo-first-order reaction. The kinetics can be calculated with $-In(C_t/C_0) = k_{app}t$, in which k_{app}, C_0 and C_t represent the apparent reaction rate constant, the PTBP concentration at initial time and the illumination time t, respectively [55]. The specific fitting curves are shown in Fig. 8c, and their reaction rate constants are depicted in Fig. 8d. It is obviously seen that 1 wt% h-BN/$Bi_4O_5Br_2$-LMs has the highest value of k_{app} (0.02004 min^{-1}), which is nearly four times larger than that of the pure $Bi_4O_5Br_2$-LMs (0.00527 min^{-1}). This indicates that the significant role of loaded h-BN in the enhanced photocatalytic degradation activity of the composite.

Additionally, the photocatalytic activity was also evaluated using APAP as a model pollutant under visible-light irradiation and the result is shown in Fig. 8b. It is clearly observed that the degradation activity of 1.0 wt% h-BN/$Bi_4O_5Br_2$-LMs is better than that of pure $Bi_4O_5Br_2$-LMs which is similar to the photocatalytic degradation of PTBP. Norfloxacin, as an antibiotic, caused environmental pollution by different ways and aroused the concern of researchers. In Fig. S5, while the photocatalyst loaded with 1.0 wt% h-BN photodegrades nearly 90% of NOR in 5 min, the pure $Bi_4O_5Br_2$-LMs degrades only less than 60%. Therefore, it can propose that the as-prepared samples are efficient visible-light-driven photocatalysts and have a potential application in environmental pollutants removal.

3.3.2. Reusability and stability

Reusability and stability of catalysts are important issues in terms of the practical application. In this study, the constructed photocatalysts were collected after the photocatalytic reaction and reused four times under the same conditions. As can be seen from Fig. 8e, the photocatalytic activity decreases by only about 7% after four cycles in degradation, indicating that the prepared catalyst has the rather high reusability. The slightly deactivation might be partly caused by inevitable collection of catalyst during the recovery process. In addition, Fig. 8f shows the XRD

pattern of h-BN/$Bi_4O_5Br_2$-LMs before and after the photodegradation, the unapparent change of crystalline structure demonstrates that h-BN/$Bi_4O_5Br_2$-LMs has high stability. The described consequences declare that the h-BN/$Bi_4O_5Br_2$-LMs synthesized by the facile microemulsion-mediated method is stable and could be used in practical application.

3.4. The underlying photocatalytic mechanism of the as-prepared photocatalyst

3.4.1. Roles of reactive species

Effect of different scavengers on photocatalytic degradation of PTBP under the same condition was investigated to explore the reactive species of the sample. The scavengers include isopropanol (IPA) for hydroxyl radicals ($\bullet$OH), 4-hydroxy-2, 2, 6, 6-tetramethylpiperidinyloxy (TEMPOL) for superoxide radicals ($\bullet O_2^-$) and ammonium oxalate (AO) for holes (h^+) [40,56,57]. The lower photocatalytic efficiency caused by the effect of the scavenger, the greater importance of the scavenger corresponding to the reactive specie is in the degradation system. As shown in Fig. S6, inhibitions of the photocatalytic performance are observed with the addition of TEMPOL and AO, which means that $\bullet O_2^-$ and h^+ play a key role in the photocatalysis. Furthermore, the addition of IPA does not influence the degradation efficiency, which infers that $\bullet$OH is not the main active species in this system.

The obtained results of the scavenger experiments were further verified by the characterization of electron paramagnetic resonance (EPR). In Fig. 9a, it is clearly seen that there is no obvious difference between the active species of the pure $Bi_4O_5Br_2$-LMs and the composite catalyst. The characteristic peaks of superoxide radical indicate the presence of $\bullet O_2^-$ during the single-electron reduction process. And the effect of $\bullet$OH was also re-evaluated by EPR technique, but no obvious characteristic peaks are observed in Fig. 9b. Based on the results, $\bullet O_2^-$ and h^+ are both the main reactive species in this photocatalytic degradation system.

3.4.2. Potential degradation mechanisms

To explain the improved photocatalytic activity of h-BN/$Bi_4O_5Br_2$-LMs, the band structure and electron density of h-BN and $Bi_4O_5Br_2$-LMs were calculated by density functional theory (DFT). For $Bi_4O_5Br_2$-LMs (Fig. 10), while the CB edge is mainly composed of Bi 6p, VB edge is basically made up of O 2p, Br 4p, Br 4s, O 2 s and Bi 6 s orbits. Because O atom and close Br
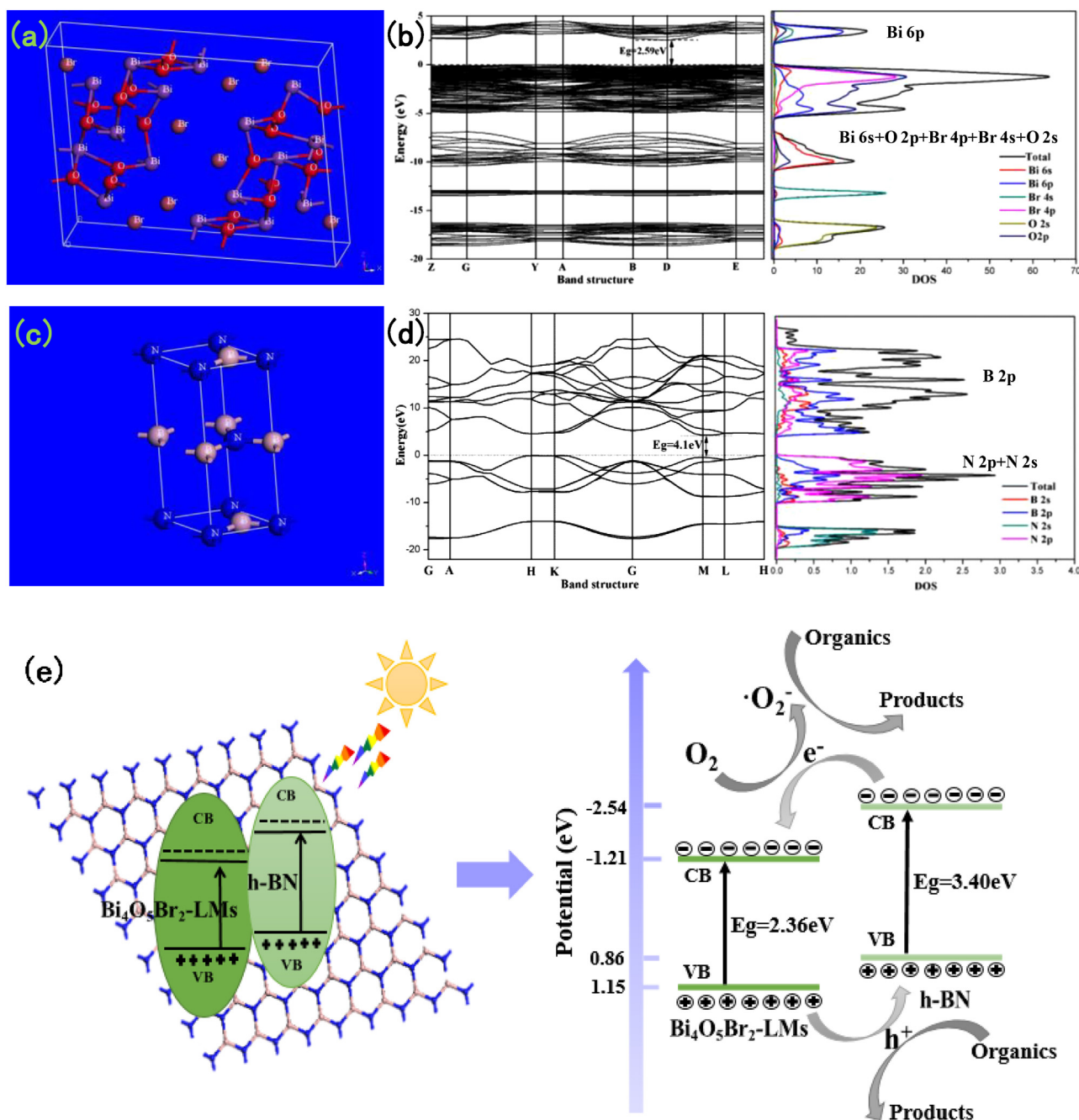
Fig. 10. Crystal structures, calculated band structures and density of states of (a, b) $Bi_4O_5Br_2$-LMs and (c, d) h-BN. (e) Schematic of the separation and transportation of photo-induced charges in the h-BN/$Bi_4O_5Br_2$-LMs composites combined with the possible photocatalytic degradation mechanism.

and Bi atoms hydride together very well in the VB, causing that VB electrons are difficult to be excited. Additionally, the large hybrid electron density formed by O, Br atoms and adjacent Bi atoms also enhances the electrostatic attraction between the nuclear and electrons. The lower electron density of the Bi atoms with close O and Br atoms in the CB makes the CB electrons easy to migrate to the surface of $Bi_4O_5Br_2$-LMs, thus effectively avoiding the recombination of electron-hole pairs. In comparison with $Bi_4O_5Br_2$-LMs, the CB edge of h-BN mainly consists of B 2p orbit, and the edge of VB is basically composed of N 2p and N 2 s orbits. The N atoms of VB have a lower hybridization with the adjacent B atoms, indicating that VB electrons are easily to be excited. What is more, due to the complex electron density between B atoms and adjacent N atoms in the CB, the CB electrons mostly migrate to

the inside of h-BN, leading to high recombination of electron-hole pairs. Therefore, h-BN/$Bi_4O_5Br_2$-LMs will reduce the hybrid electron density of h-BN in the CB, and thus the CB electrons of h-BN migrate to the surface of $Bi_4O_5Br_2$-LMs, preventing recombination of electron-hole pairs. At the same time, the existence of h-BN will reduce the composite electron density of the VB of $Bi_4O_5Br_2$-LMs, which is in favor of electrons transferring from VB to the CB. Therefore, the successful h-BN loading on the $Bi_4O_5Br_2$-LMs can effectively promote the separation of electron-hole pairs, thereby improving the photocatalytic activity of h-BN/$Bi_4O_5Br_2$-LMs.

On the basis of the above mentioned experimental and calculative results, the significant improvement of photocatalytic degradation efficiencies for pollutants could be mainly attributed to the synergistic effect between $Bi_4O_5Br_2$-LMs and
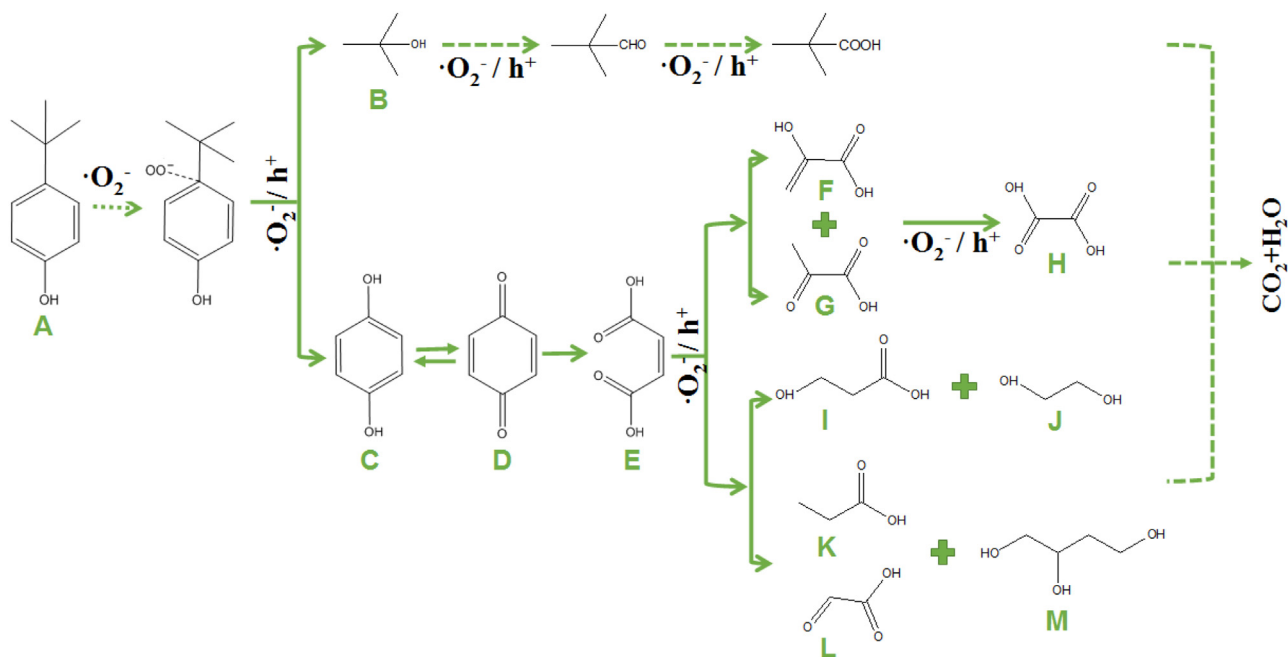
Fig. 11. Proposed photocatalytic degradation pathways of PTBP on the h-BN/Bi$_4$O$_5$Br$_2$-LMs under visible-light irradiation (the dashed lines are a theoretical analysis).

graphene-analogue h-BN. The proposed photocatalytic degradation mechanism is vividly illustrated in Fig. 10e.

On the one hand, layered architecture of graphene-analogue h-BN, as a promoter, can accelerate the surface charge migration of Bi$_4$O$_5$Br$_2$-LMs after the heterojunction is constructed, so as to suppress the recombination of electron-hole pairs. On the other hand, the presence of the ionic-liquid and 3D microspherical structure of Bi$_4$O$_5$Br$_2$-LMs are in favor of h-BN dispersion in the synthetic system, thus reducing the occurrence of agglomeration phenomenon and forming a tight structure between h-BN and Bi$_4$O$_5$Br$_2$-LMs. When the h-BN/Bi$_4$O$_5$Br$_2$-LMs are irradiated, electrons are excited and transferred from VB to CB, so holes are left on the VB. The electrons of h-BN in the CB will transfer to the Bi$_4$O$_5$Br$_2$-LMs and the holes will be toward the shift to the opposite direction, that is, from the VB of Bi$_4$O$_5$Br$_2$-LMs migrate to the VB of h-BN. Thus an efficient separation of photoinduced electron-hole pairs can be achieved in the formed heterojunction between semiconductors with appropriate band potentials [58]. The VB values of Bi$_4$O$_5$Br$_2$-LMs and h-BN were measured by XPS valence spectroscopy (Fig. S7). While the VB of h-BN (0.86 eV) is less positive to oxidize OH$^-$ or H$_2$O to •OH for the standard reduction potential of •OH/H$_2$O (2.27 eV) or •OH/OH$^-$ (2.38 eV) [59]. The CB value of sample is calculated by the formula E$_{CB}$ = E$_{VB}$-E$_g$, where the E$_g$ is the band gap and can be attained from the results of DRS, considering the E^0 (O$_2$/•O$_2^-$) is about −0.046 eV [60,61], the CB value of Bi$_4$O$_5$Br$_2$-LMs (−1.21 eV) is negative enough to reduce the O$_2$ to •O$_2^-$. Therefore, the formed active species h$^+$ and •O$_2^-$ directly oxidize the organic molecules in aqueous solution under visible-light irradiation.

3.4.3. Identification of intermediate products

Theoretical calculation of frontier electron densities (FED) was utilized to correctly characterize positions of free radical attraction. According to Frontier Orbital Theory, positions with higher values of 2FED$^2_{HOMO}$ are more easily subject to electron extraction. And the higher value of FED$^2_{HOMO}$ + FED$^2_{LUMO}$ presents that the position is more likely to be attacked by free radicals [62]. Based on the intercomparison of these data of PTBP (Fig. S8) in Table S1,

in terms of 2FED$^2_{HOMO}$, 5C and 11O have the highest values; 2C, 3C, 8C and 10C have the relatively higher values, so these positions possess a fair chance of electron extraction. For the value of FED$^2_{HOMO}$ + FED$^2_{LUMO}$, while 8C and 10C are the highest, 1C, 3C, 4C and 6C are the relatively higher, where may be more susceptible to free radical attack. The results provide theoretical basis for the derivation of proposed photocatalytic degradation pathways.

The photocatalytic products of PTBP were analyzed by GC–MS with EI full-scan patterns. The organic compounds were identified based on the values of m/z, and compared them with the U.S. National Institute of Standards and Technology (NIST) library (matching ratio >60%). The structure, molecular weight and toxicity (if available) of the compounds are listed in Table 1.

According to the FED calculation and the identified products by GC–MS, the main photocatalytic degradation pathways of PTBP are considered to be the conjugated addition and oxidation reaction. The compounds listed (letter identification) in Fig. 11 are obtained under TMS derivatization condition except these C, D and M. In the oxygen-containing aqueous solution, the photocatalyst is excited and generates electrons under visible-light irradiation, these electrons can be trapped by O$_2$ to generate •O$_2^-$ in the aerated solution. The present of •O$_2^-$ in the reaction system leads to the conjugated addition to form the radical 4-*tert*-butylphenol (•OO- as shown in Fig. 11). As *ortho*-4-*tert*-butylphenoxy group is very active, *tert*-butyl alcohol (B) and 1,4-benzenediol (hydroquinone, C) can be generated. The former executes oxidation reaction to generate *tert*-butyl aldehyde and *tert*-butyric acid, as illustrated in Fig. 11. The latter carries out a ring-opening reaction in the existence of •O$_2^-$ and h$^+$ which are easily inclined to attack quinone. After the aromatic ring opening, maleic acid (E) might be easily produced, which can be further oxidized to smaller products in this reaction system. The photocatalytic degradation products (F-M) of PTBP with low molecular mass are identified in Table 1. LD$_{50}$ values for some of degradation products and PTBP are also listed in the table. It could be deduced that the majority of degradation products are less harmful than their parent to environment due to high LD$_{50}$ values. And PTBP can be degraded to some small innocuous molecules by photocatalysis under visible-light irradiation.

Table 1
The photocatalytic degradation intermediates and products of PTBP detected by GC–MS and their toxicity.

Product	m/z	Name	Toxicity LD$_{50}$ (Rat) *	Molecular Structure
A	150	4-*tert*-butylphenol	3250 μg/kg	
B	74	2-methyl-2-propanol	3500 mg/kg	
C	110	Hydroquinone	320 mg/kg	
D	108	Cyclohexa-2,5-diene-1,4-dione	320 mg/kg	
E	116	Maleic acid	708 mg/kg	
F	89	2-hydroxyacrylic acid	NA	
G	89	2-oxopropanoic acid	NA,metabolism of glucose	
H	90	Oxalic acid	600 mg/kg	
I	90	3-hydroxypropanoic acid	NA	
J	62	Ethane-1,2-diol	1525 mg/kg	
K	74	Propionic acid	NA Biological uses	
L	74	Formyl formic acid	NA	
M	106	Butane-1,2,4-triol	NA Biotech. synthesis	

*Most of the toxicity data are obtained from Wikipedia (https://en.wikipedia.org/wiki/); NA means the toxicity data are not available.

4. Conclusion

In this study, the novel graphene-analogue h-BN/Bi$_4$O$_5$Br$_2$-LMs heterojunction photocatalyst was successfully synthesized by microemulsion-mediated method. In comparison to pure Bi$_4$O$_5$Br$_2$-LMs and h-BN, h-BN/Bi$_4$O$_5$Br$_2$-LMs exhibited a high photocatalytic activity for the photodegradation of PTBP under visible-light irradiation. The superior catalytic activity was 1 wt% h-BN/Bi$_4$O$_5$Br$_2$-LMs, by which about 97% of PTBP was photodegraded within 150 min. The photocurrent experiments showed that the photocurrent density of 1.0 wt% h-BN/Bi$_4$O$_5$Br$_2$-LMs was four times higher than that of pure Bi$_4$O$_5$Br$_2$-LMs. It demonstrates that the

excellent performance can be ascribed to the formed heterostructure between h-BN and $Bi_4O_5Br_2$-LMs, which reinforce separation efficiency of photogenerated electron-hole pairs. Moreover, the results of scavenger experiment and EPR measurement conformed that $\bullet O_2^-$ and h^+ are the main reactive species in the photocatalytic process. The probable degradation products of PTBP were identified by GC/MS, the proposed degradation pathway was described by combining the frontier electron density calculation, which indicates that the conjugated addition and oxidation reaction are the main photocatalytic degradation mechanism of PTBP. This research finding will be useful to acquire a highly efficient visible-light-driven photocatalyst and might open a wide practical application in the field of environmental remediation and energy conversion.

Acknowledgements

Appendix A. Supplementary data

Supplementary data associated with this article can be found, in the online version, at http://dx.doi.org/10.1016/j.apcatb.2017.04.002.

References

[1] R.K. Nath, M.F.M. Zain, M. Jamil, Renew. Sustainable Energy Rev. 62 (2016) 1184–1194.
[2] R.K. Ibrahim, M. Hayyan, M.A. AlSaadi, A. Hayyan, S. Ibrahim, Environ. Sci. Pollut. R. 23 (2016) 13754–13788.
[3] D. Malwal, P. Gopinath, Crit. Rev. Environ. Sci. Technol. 46 (2016) 500–534.
[4] C. Yu, W. Zhou, H. Liu, Y. Liu, D.D. Dionysiou, Chem. Eng. J. 287 (2016) 117–129.
[5] K.M. Lee, C.W. Lai, K.S. Ngai, J.C. Juan, Water Res. 88 (2016) 428–448.
[6] W. Wang, F. Huang, X. Lin, J. Yang, Catal. Commun. 9 (2008) 8–12.
[7] D.J. Mao, X.M. Lu, Z.F. Jiang, J.M. Xie, X.F. Lu, W. Wei, A.M.S. Hossain, Mater. Lett. 118 (2014) 154–157.
[8] M.A. Gondal, X.F. Chang, M.A. Ali, Z.H. Yamani, Q. Zhou, G.B. Ji, Appl. Catal. A-Gen. 397 (2011) 192–200.
[9] J. Xu, W. Meng, Y. Zhang, L. Li, C. Guo, Appl. Catal. B: Environ. 107 (2011) 355–362.
[10] Y.F. Fang, Y.P. Huang, J. Yang, P. Wang, G.W. Cheng, Environ. Sci. Technol. 45 (2011) 1593–1600.
[11] L. Zhang, X.F. Cao, X.T. Chen, Z.L. Xue, J. Colloid Interface Sci. 354 (2011) 630–636.
[12] J.Y. Liu, Y. Bai, P.Y. Luo, P.Q. Wang, Catal. Commun. 42 (2013) 58–61.
[13] J. Di, J. Xia, M. Ji, S. Yin, H. Li, H. Xu, Q. Zhang, H. Li, J. Mater. Chem. A 3 (2015) 15108–15118.
[14] W. Zhao, Y. Liu, Z.B. Wei, S.G. Yang, H. He, C. Sun, Appl. Catal. B: Environ. 185 (2016) 242–252.
[15] X. Xiao, C. Liu, R. Hu, X. Zuo, J. Nan, L. Li, L. Wang, J. Mater. Chem. 22 (2012) 22840–22843.
[16] J. Xia, Y. Ge, J. Di, L. Xu, S. Yin, Z. Chen, P. Liu, H. Li, J. Colloid Interface Sci. 473 (2016) 112–119.
[17] J. Wang, Y. Yu, L. Zhang, Appl. Catal. B: Environ. 136 (2013) 112–121.
[18] J. Di, J. Xia, S. Yin, H. Xu, M. He, H. Li, L. Xu, Y. Jiang, RSC Adv. 3 (2013) 19624–19631.
[19] Y. Bai, L.Q. Ye, L. Wang, X. Shi, P.Q. Wang, W. Bai, P.K. Wong, Appl. Catal. B: Environ. 194 (2016) 98–104.
[20] N. Tian, Y.H. Zhang, C.Y. Liu, S.X. Yu, M. Li, H.W. Huang, RSC Adv. 6 (2016) 10895–10903.
[21] D. Jiang, X. Du, D. Chen, Y. Li, N. Hao, J. Qian, H. Zhong, T. You, K. Wang, Carbon 102 (2016) 10–17.
[22] M. Wang, M.H. Li, L.Q. Xu, L.C. Wang, Z.C. Ju, G.D. Li, Y.T. Qian, Catal. Sci. Technol. 1 (2011) 1159–1165.
[23] K. Novoselov, D. Jiang, F. Schedin, T. Booth, V. Khotkevich, S. Morozov, Proc. Natl. Acad. Sci. U. S. A. 102 (2005) 10451–10453.
[24] Q. Peng, W. Ji, S. De, Comput. Mater. Sci. 56 (2012) 11–17.
[25] Y. Lin, T.V. Williams, W. Cao, H.E. Elsayed-Ali, J.W. Connell, J. Phys. Chem. C 114 (2010) 17434–17439.
[26] Y. Liu, S. Bhowmick, B.I. Yakobson, Nano Lett. 11 (2011) 3113–3116.
[27] A. Nag, K. Raidongia, K.P. Hembram, R. Datta, U.V. Waghmare, C. Rao, ACS Nano 4 (2010) 1539–1544.
[28] A.K. Geim, I.V. Grigorieva, Nature 499 (2013) 419–425.
[29] Y.F. Sun, Y. Gao, F.C. Lei, Y. Xie, Chem. Soc. Rev. 44 (2015) 623–636.
[30] H.T. Wang, H.T. Yuan, S.S. Hong, Y.B. Li, Y. Cui, Chem. Soc. Rev. 44 (2015) 2664–2680.
[31] J. Di, J. Xia, M. Ji, B. Wang, S. Yin, Q. Zhang, Z. Chen, H. Li, Appl. Catal. B: Environ. 183 (2016) 254–262.
[32] D. Liu, Z. Jiang, C. Zhu, K. Qian, Z. Wu, J. Xie, Dalton Trans. 45 (2016) 2505–2516.
[33] O.P. Heemken, H. Reincke, B. Stachel, N. Theobald, Chemosphere 45 (2001) 245–259.
[34] K. Inoue, Y. Yoshie, S. Kondo, Y. Yoshimura, H. Nakazawa, J. Chromatogr. A 946 (2002) 291–294.
[35] C.H. Koh, J.S. Khim, D.L. Villeneuve, K. Kannan, J.P. Giesy, Environ. Pollut. 142 (2006) 39–47.
[36] A. Barse, T. Chakrabarti, T.K. Ghosh, A.K. Pal, S.B. Jadhao, Pestic. Biochem. Phys. 86 (2006) 172–179.
[37] F. Yang, Z. Abdel-Malek, R.E. Boissy, In vitro cell, Deve-An 35 (1999) 566–570.
[38] F. Yang, R. Sarangarajan, I.C. Le Poole, E.E. Medrano, R.E. Boissy, J. Invest. Dermatol. 114 (2000) 157–164.
[39] T. Toyama, N. Momotani, Y. Ogata, Y. Miyamori, D. Inoue, K. Sei, K. Mori, S. Kikuchi, M. Ike, Appl. Environ. Microbiol. 76 (2010) 6733–6740.
[40] X. Xiao, C. Xing, G. He, X. Zuo, J. Nan, L. Wang, Appl. Catal. B: Environ. 148 (2014) 154–163.
[41] J. Xia, M. Ji, J. Di, B. Wang, S. Yin, Q. Zhang, M. He, H. Li, Appl. Catal. B: Environ. 191 (2016) 235–245.
[42] J. Xia, J. Di, H. Li, H. Xu, H. Li, S. Guo, Appl. Catal. B: Environ. 181 (2016) 260–269.
[43] Y. Wang, K. Deng, L. Zhang, J. Phys. Chem. C 115 (2011) 14300–14308.
[44] D. Mao, S. Ding, L. Meng, Y. Dai, C. Sun, S. Yang, H. He, Appl. Catal. B: Environ. 207 (2017) 153–165.
[45] L. Wang, S.-Q. Ni, C. Guo, Y. Qian, J. Mater. Chem. A 1 (2013) 6379–6387.
[46] J. Xiong, W. Zhu, H. Li, W. Ding, Y. Chao, P. Wu, S. Xun, M. Zhang, H. Li, Green Chem. 17 (2015) 1647–1656.
[47] W. Zhao, Y. Liu, Z. Wei, S. Yang, H. He, C. Sun, Appl. Catal. B: Environ. 185 (2016) 242–252.
[48] M. Shanmugam, R. Jacobs-Gedrim, C. Durcan, B. Yu, Nanoscale 5 (2013) 11275–11282.
[49] X. Fu, Y. Hu, T. Zhang, S. Chen, Appl. Surf. Sci. 280 (2013) 828–835.
[50] J. Di, J. Xia, Y. Ge, H. Li, H. Ji, H. Xu, Q. Zhang, H. Li, M. Li, Appl. Catal. B: Environ. 168 (2015) 51–61.
[51] S.G. Meng, X.J. Ye, X.F. Ning, M.L. Xie, X.L. Fu, S.F. Chen, Appl. Catal. B: Environ. 182 (2016) 356–368.
[52] K.T. Park, K. Terakura, N. Hamada, J. Phys. C: Solid State Phys. 20 (1987) 1241.
[53] J. Hu, W. Fan, W. Ye, C. Huang, X. Qiu, Appl. Catal. B: Environ. 158 (2014) 182–189.
[54] Q. Xiang, J. Yu, M. Jaroniec, J. Phys. Chem. C 115 (2011) 7355–7363.
[55] J. Xu, W. Meng, Y. Zhang, L. Li, C. Guo, Appl. Catal. B: Environ. 107 (2011) 355–362.
[56] L. Jinhai, M. Han, Y. Guo, F. Wang, L. Meng, D. Mao, S. Ding, C. Sun, Appl. Catal. A-Gen. 524 (2016) 105–114.
[57] D. Mao, A. Yu, S. Ding, F. Wang, S. Yang, C. Sun, H. He, Y. Liu, K. Yu, Appl. Surf. Sci. 389 (2016) 742–750.
[58] X. Zhang, L.Z. Zhang, T.F. Xie, D.J. Wang, J. Phys. Chem. C 113 (2009) 7371–7378.
[59] Y. Guo, J. Li, Z. Gao, X. Zhu, Y. Liu, Z. Wei, W. Zhao, C. Sun, Appl. Catal. B: Environ. 192 (2016) 57–71.
[60] D. Wang, T. Kako, J. Ye, J. Am. Chem. Soc. 130 (2008) 2724–2725.
[61] L. Ye, J. Chen, L. Tian, J. Liu, T. Peng, K. Deng, L. Zan, Appl. Catal. B: Environ. 130 (2013) 1–7.
[62] Y. Li, Z.Q. Gao, Y.F. Ji, X.B. Hu, C. Sun, S.G. Yang, L.H. Wang, Q.G. Wang, D. Fang, J. Hazard. Mater. 285 (2015) 127–136.